Unsupervised Discovery of Object-Centric Neural Fields

Anonymous authors
Paper under double-blind review

Abstract

We study inferring 3D object-centric scene representations from a single image. While recent methods have shown potential in unsupervised 3D object discovery, they are limited in generalizing to unseen spatial configurations. This limitation stems from the lack of translation invariance in their 3D object representations. Previous 3D object discovery methods entangle objects' intrinsic attributes like shape and appearance with their 3D locations. This entanglement hinders learning generalizable 3D object representations. To tackle this bottleneck, we propose the unsupervised discovery of Object-Centric neural Fields (uOCF), which integrates translation invariance into the object representation. To allow learning object-centric representations from limited real-world images, we further introduce an object prior learning method that transfers object-centric prior knowledge from a synthetic dataset. To evaluate our approach, we collect four new datasets, including two real kitchen environments. Extensive experiments show that our approach significantly improves generalization and sample efficiency, and enables unsupervised 3D object discovery in real scenes. Notably, uOCF demonstrates zero-shot generalization to unseen objects from a single real image. Project page: https://anonymous.4open.science/w/uOCF-TMLR25-58D0/.

1 Introduction

Creating factorized, object-centric 3D scene representations is a fundamental ability in human vision and a long-standing topic of interest in computer vision and machine learning. Some recent work has explored unsupervised learning of 3D factorized scene representations from images alone (Stelzner et al., 2021; Yu et al., 2022; Smith et al., 2023; Jia et al., 2023). These methods have delivered promising results in 3D object discovery and reconstruction from a simple synthetic image.

However, existing methods fail to generalize to unseen spatial configurations and objects. A fundamental bottleneck is that their representations lack the invariance to the 3D positions of the objects. In particular, existing methods represent 3D objects as implicit functions in the viewer's coordinate frame, so that any change related the coordinate frame (e.g., slight changes in an object's location or subtle camera movements) may lead to significant changes in the object representation even if the object remains the same. Therefore, existing methods do not generalize when an object appears at an unseen location during inference.

To address this fundamental bottleneck, we propose the unsupervised discovery of Object-Centric neural Fields (uOCF). Unlike existing methods, uOCF explicitly infers an object's 3D location, disentangling it from the object's latent representation. This design builds translation invariance into the object representation, so that the object's latent only represents the intrinsics of the object (e.g., shape and appearance). This design significantly improves generalization. As showcased in Figure 1, uOCF can generalize to unseen real-world scenes. We train uOCF on sparse multi-view images without object annotations. During inference, uOCF takes in a single image and generates a set of object-centric neural radiance fields (NeRFs) (Mildenhall et al., 2020) and a background NeRF.

Another advantage of our translation-invariant 3D object representation is that it facilitates learning 3D object priors from simple scenes and generalizes to more complex scenes with unseen spatial configurations and objects. This further boosts sample efficiency and thus it is particularly beneficial when we deal with real scenes where training data is often limited. We introduce an object prior learning method to this end.

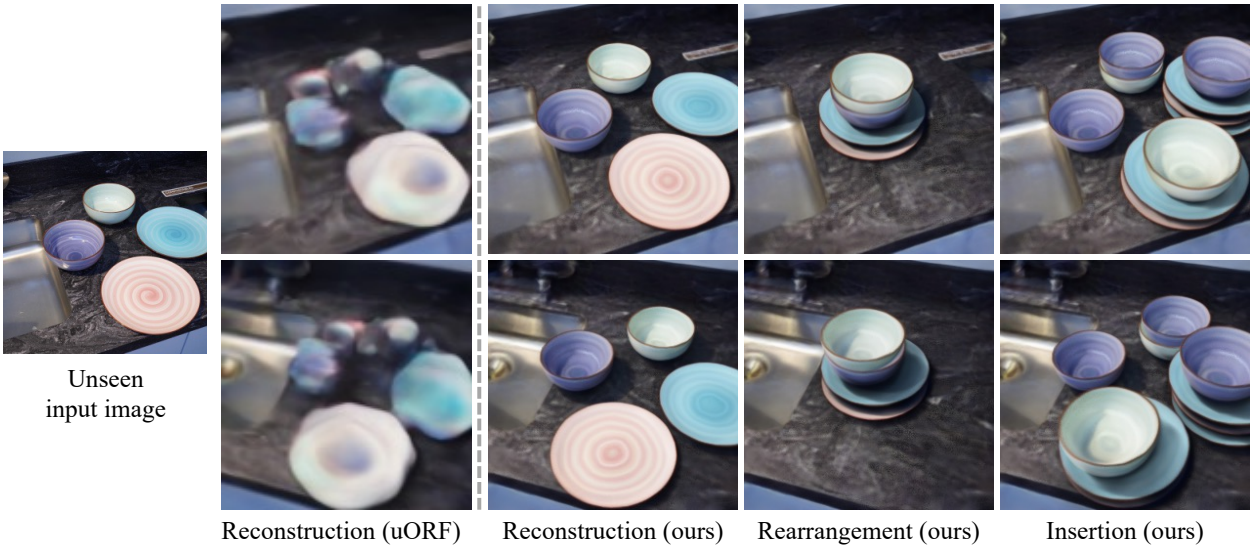

Figure 1: We propose the unsupervised discovery of Object-Centric neural Fields (uOCF), which infers factorized 3D scene representations from an unseen real image, thus enabling scene reconstruction and manipulation from novel views. We compare uOCF with the state-of-the-art method, uORF (Yu et al., 2022).

To evaluate our approach, we introduce new challenging datasets for 3D object discovery, including two real kitchen datasets and two synthetic room datasets. The two real datasets feature real-world kitchen backgrounds and objects from multiple categories. The synthetic room datasets feature furniture with diverse, realistic shapes and textures. Across all these datasets, uOCF yields high-fidelity discovery of object-centric neural fields, allowing applications such as unsupervised 3D object segmentation and scene manipulation from a real image. uOCF shows strong generalization to unseen spatial configurations and high sample efficiency, and we showcase that it even allows *zero-shot* 3D object discovery on a few simple real scenes with unseen objects. In summary, our contributions are threefold:

- First, we highlight the overlooked role of translation invariance in unsupervised 3D object discovery. We instantiate the idea by proposing the unsupervised discovery of Object-Centric neural Fields (uOCF), which builds translation invariance to the object representation.
- Second, we introduce a 3D object prior learning method, which leverages uOCF's translation-invariant property to learn category-agnostic object priors from simple scenes and generalize to different object categories and scene layouts.
- Lastly, we collect four challenging datasets, Room-Texture, Room-Furniture, Kitchen-Matte, and Kitchen-Shiny, and show that uOCF significantly outperforms existing methods on these datasets, unlocking zero-shot, single-image object discovery. All code and data will be made public.

2 Related Works

Unsupervised object discovery. Prior to the rise of deep learning, traditional methods for object discovery (often referred to as co-segmentation) primarily aimed at locating visually similar objects across a collection of images (Sivic et al., 2005; Russell et al., 2006), where objects are defined as visual words or clusters of patches (Grauman & Darrell, 2006; Joulin et al., 2010). This clustering concept was later incorporated into deep learning techniques for improved grouping results (Li et al., 2019; Vo et al., 2020). The incorporation of deep probabilistic inference propelled the field towards factorized scene representation learning (Eslami et al., 2016). These methods decompose a visual scene into several components, where objects are often modeled as latent codes that can be decoded into image patches (Kosiorek et al., 2018; Crawford & Pineau, 2019; Jiang et al., 2020; Lin et al., 2020), scene mixtures (Greff et al., 2016; 2017; 2019; Burgess et al., 2019; Engelcke et al., 2019; Locatello et al., 2020; Biza et al., 2023; Didolkar et al., 2023), or layers (Monnier et al., 2021). Despite their efficacy in scene decomposition, they do not model the objects' 3D nature.

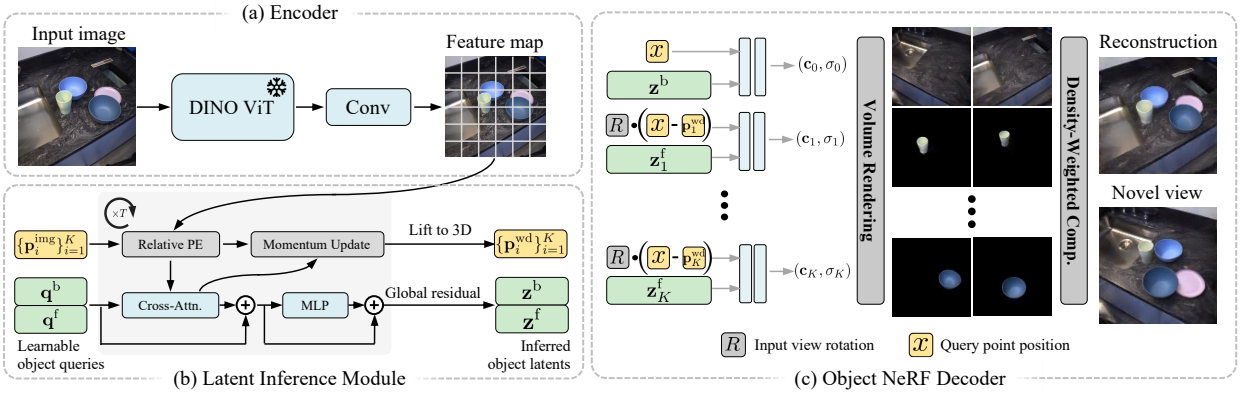

Figure 2: With a single forward pass, uOCF processes a single image input to infer a set of object-centric radiance fields along with their 3D locations and background radiance field. uOCF is trained on sparse multi-view images from a collection of scenes and uses a single image as input during inference.

Unsupervised 3D object discovery. To model the 3D nature of scenes and objects, some recent works tried to learn 3D-aware representations from multi-view images of a single-scene (Liang et al., 2022) or of large datasets for generalization (Eslami et al., 2018; Chen et al., 2020; Sajjadi et al., 2022), while the latest research emphasizes the single-image inference of object-centric factorized scene representations (Stelzner et al., 2021; Yu et al., 2022; Smith et al., 2023). Notably, Yu et al. (2022) propose the unsupervised discovery of object radiance fields (uORF) from a single image. Later literature improves the efficiency (Smith et al., 2023) and segmentation (Jia et al., 2023). However, their object representations suffer from the lack of object translation invariance. Our work is the first to incorporate translation invariance to significantly improve generalization and sample efficiency.

Object-centric 3D reconstruction. Decomposing visual scenes on an object-by-object basis and estimating their semantic/geometric attributes has been explored in several recent works (Wu et al., 2017; Yao et al., 2018; Kundu et al., 2018; Ost et al., 2021). Some approaches, such as AutoRF (Müller et al., 2022), successfully reconstruct specific objects (*e.g.*, cars) from annotated images. Others decompose visual scenes into the background and individual objects represented by neural fields (Yang et al., 2021; Wu et al., 2022). Our work differs because of its emphasis on unsupervised learning. Another line of recent work focuses on lifting 2D segmentation to reconstructed 3D scenes (Fan et al., 2022; Cen et al., 2023a;b). In contrast, our work aims at single-image inference, whereas these studies concentrate on multi-view reconstruction.

Generative neural fields. Neural fields have revolutionized 3D scene modeling. Early works have shown promising geometric representations (Sitzmann et al., 2019; Park et al., 2019). The seminal work on neural radiance fields (Mildenhall et al., 2020) has opened up a burst of research on neural fields. We refer the reader to recent survey papers (Tewari et al., 2020; Xie et al., 2022) for a comprehensive overview. In particular, compositional generative neural fields such as GIRAFFE (Niemeyer & Geiger, 2021) and others (Nguyen-Phuoc et al., 2020; Wang et al., 2023b) also allow learning object representations from image collections. Yet, they target unconditional generation and cannot tackle inference.

3 Approach

Given a single input image, our goal is to infer object-centric radiance fields (i.e., each discovered object is represented in its local object coordinate rather than the world or the viewer coordinates) and the objects' 3D locations. The object-centric design not only boosts generalizability due to representation invariance, but also allows learning object priors from scenes with different spatial layouts and compositional configurations. The following provides an overview of our approach and then introduces the technical details.

3.1 Model Overview

As shown in Figure 2, uOCF consists of an encoder, a latent inference module, and a decoder.

Encoder. From an input image $\mathbf{I}$, the encoder extracts a feature map $\mathbf{f} \in \mathbb{R}^{N \cdot C}$, where $N = H \cdot W$ is the spatial size of the feature map and C represents the number of channels. We set it as a frozen DINOv2-ViT (Oquab et al., 2023) followed by two convolutional layers.

Latent inference module. The latent inference module infers the latent representation and position of the objects in the underlying 3D scene from the feature map. We assume that the scene is composed of a background environment and no more than K foreground objects. Therefore, the output includes a background latent $\mathbf{z}^{\text{b}} \in \mathbb{R}^{1\times D}$ and a set of foreground object latent $\mathbf{z}^{\text{f}} = [\mathbf{z}_1^{\text{f}T}\ \mathbf{z}_2^{\text{f}T}\ \cdots\ \mathbf{z}_K^{\text{f}T}]^T \in \mathbb{R}^{K\times D}$ with their corresponding positions $\{\mathbf{p}_i^{\text{wd}}\}_{i=1}^K$, where $\mathbf{p}_i^{\text{wd}} \in \mathbb{R}^3$ denotes a position in the world coordinate. Note that some object latent may be empty when the scene has $< K$ objects.

Decoder. Our decoder employs the conditional NeRF formulation $g(\mathbf{x}|\mathbf{z})$, which takes the 3D location $\mathbf{x}$ and the latent $\mathbf{z}$ as input and generates the radiance color and density for rendering. We use two MLPs, g^{b} and g^{f}, for the background environment and the foreground objects, respectively.

3.2 Object-Centric 3D Scene Modeling

Object-centric latent inference. Our Latent Inference Module (LIM) aims at binding a set of learnable object queries ($\mathbf{q}^{\text{f}} = [\mathbf{q}_1^{\text{f}T}\ \mathbf{q}_2^{\text{f}T}\ \cdots\ \mathbf{q}_K^{\text{f}T}]^T \in \mathbb{R}^{K\times D}$) to the visual features of each foreground object, and another query to the background features ($\mathbf{q}^{\text{b}} \in \mathbb{R}^{1\times D}$). The binding is modeled via the cross-attention mechanism with learnable linear functions $\mathcal{K}^{\text{b}}, \mathcal{K}^{\text{f}}, \mathcal{Q}^{\text{b}}, \mathcal{Q}^{\text{f}}, \mathcal{V}^{\text{b}}, \mathcal{V}^{\text{f}}$:

$$\mathbf{A}_{i,j} = \frac{\exp(\mathbf{M}_{i,j})}{\sum_k \exp(\mathbf{M}_{i,k})}, \quad \text{where} \quad \mathbf{M} = \frac{1}{\sqrt{D^s}} \begin{bmatrix} \mathcal{Q}^{\text{b}}(\mathbf{q}^{\text{b}}) \cdot \mathcal{K}^{\text{b}}(\mathbf{f})^T \\ \mathcal{Q}^{\text{f}}(\mathbf{q}^{\text{f}}) \cdot \mathcal{K}^{\text{f}}(\mathbf{f})^T \end{bmatrix}^T \in \mathbb{R}^{N\times(K+1)}. \tag{1}$$

We then calculate the update signals for queries via an attention-weighted mean of the input:

$$\mathbf{u}^{\text{b}} = (\mathbf{W}_{(:,1)})^T \cdot \mathcal{V}^{\text{b}}(\mathbf{f}) \in \mathbb{R}^{1\times D}; \quad \mathbf{u}^{\text{f}} = (\mathbf{W}_{(:,2:)})^T \cdot \mathcal{V}^{\text{f}}(\mathbf{f}) \in \mathbb{R}^{K\times D}, \tag{2}$$

where $\mathbf{W}_{i,j} = \frac{\mathbf{A}_{i,j}}{\sum_l \mathbf{A}_{l,j}}$ is the normalized attention map. Queries are then updated by:

$$\mathbf{q}^{\text{b}} \leftarrow \mathbf{q}^{\text{b}} + \mathbf{u}^{\text{b}},\ \mathbf{q}^{\text{f}} \leftarrow \mathbf{q}^{\text{f}} + \mathbf{u}^{\text{f}}; \quad \mathbf{q}^{\text{b}} \leftarrow \mathbf{q}^{\text{b}} + t^{\text{b}}(\mathbf{q}^{\text{b}}),\ \mathbf{q}^{\text{f}} \leftarrow \mathbf{q}^{\text{f}} + t^{\text{f}}(\mathbf{q}^{\text{f}}), \tag{3}$$

where t^{b} and t^{f} are MLPs. We repeat this procedure for T iterations, followed by concatenating the updated object queries with the corresponding attention-weighted mean of the input feature map $\mathbf{f}$ (global residual), finally delivering the background latent $\mathbf{z}^{\text{b}}$ and foreground latent $\{\mathbf{z}_i^{\text{f}}\}_{i=1}^K$.

Our LIM is related to the Slot Attention (Locatello et al., 2020) while differs in several critical aspects. We discuss their relationship in Appendix C.1.

Object location inference. To infer objects' position along with their latent representation, we assign a normalized image position $\mathbf{p}_i^{\text{img}} \in [-1, 1]^2$ initialized as zero to each foreground object query, then iteratively update them by momentum m with the attention-weighted mean over the normalized 2D grid $\mathbf{E}^{\text{abs}} \in [-1, 1]^{N\times 2}$:

$$\mathbf{p}_i^{\text{img}} \leftarrow (\mathbf{W}_{(:,i+1)})^T \cdot \mathbf{E}^{\text{abs}} \cdot (1 - m) + \mathbf{p}_i^{\text{img}} \cdot m. \tag{4}$$

To incorporate the inferred positions, we adopt the relative positional encoding (Biza et al., 2023) $\mathbf{E}_i^{\text{pos}} := \text{concat}([\mathbf{E}^{\text{abs}} - \mathbf{p}_i^{\text{img}}, \mathbf{p}_i^{\text{img}} - \mathbf{E}^{\text{abs}}]) \in \mathbb{R}^{N\times 4}$, where concat is the concatenation along the last dimension. Then, we re-write M in Eq. (1) as:

$$M = \frac{1}{\sqrt{D^s}} \begin{bmatrix} \mathcal{Q}^{\text{b}}(\mathbf{q}^{\text{b}}) \cdot \mathcal{K}^{\text{b}}(\mathbf{f} + h_1(\mathbf{E}^{\text{abs}}))^T \\ \mathcal{Q}^{\text{f}}(\mathbf{q}_1^{\text{f}}) \cdot \mathcal{K}^{\text{f}}(\mathbf{f} + h_1(\mathbf{E}_1^{\text{pos}}))^T \\ \cdots \\ \mathcal{Q}^{\text{f}}(\mathbf{q}_K^{\text{f}}) \cdot \mathcal{K}^{\text{f}}(\mathbf{f} + h_1(\mathbf{E}_K^{\text{pos}}))^T \end{bmatrix}^T, \tag{5}$$

where $h_1 : \mathbb{R}^4 \to \mathbb{R}^D$ is a linear function.

Overall, LIM achieves a gradual binding between the queries and the objects in the scene through an iterative update of the queries and their locations. To address potential issues of duplicate object identification, we

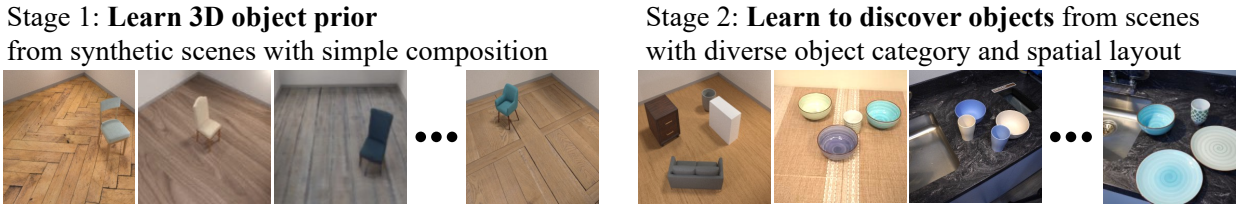

Figure 3: Our object-centric design allows learning 3D object priors that generalize across different scene configurations. We first train our model to learn 3D object priors on simple synthetic scenes (*e.g.*, single synthetic object), and then we leverage the 3D object priors to learn to discover objects in more complex scenes with different object categories and spatial layouts. Note that no object annotation is needed in either stage.

invalidate one of two similar object queries with high similarity and positional proximity by the start of the last iteration. Finally, a small bias term is added to the position to handle potential occlusion, *i.e.*, $\mathbf{p}_i^{\text{img}} \leftarrow \mathbf{p}_i^{\text{img}} + \tanh(h_2((W_{(:,i+1)})^T)) \cdot \alpha$, where scaling hyperparameter $\alpha = 0.2$ and $h_2 : \mathbb{R}^N \rightarrow \mathbb{R}^2$ is a linear function.

The 2D positions $\mathbf{p}_i^{\text{img}}$ are then unprojected into the 3D world coordinate to obtain $\mathbf{p}_i^{\text{wd}}$. To do this, we extend the rays by depth $d \cdot s_i$, where d is the depth estimated by a monocular depth estimator and $\{s_i\}_{i=1}^K$ are scaling terms predicted by a linear layer using the camera parameters and object latent as input.

Compositional neural rendering. The object positions allow us to put objects in their local coordinates rather than the viewer or world coordinates, thereby obtaining object-centric neural fields. Technically, for each 3D point $\mathbf{x}$ in the world coordinate, we transform it to the i^{th} object's local coordinate by $\mathbf{x}_i = R \cdot (\mathbf{x} - \mathbf{p}_i^{\text{wd}})$, where R denotes the input camera rotation matrix. We then retrieve the color and density of $\mathbf{x}$ in the foreground radiance fields as $(\mathbf{c}_i, \sigma_i) = g^{\text{f}}(\mathbf{x}_i | \mathbf{z}_i^{\text{f}})$ and in the background radiance field as $(\mathbf{c}_0, \sigma_0) = g^{\text{b}}(\mathbf{x} | \mathbf{z}^{\text{b}})$. These values are aggregated into the scene's composite density and color $(\overline{\mathbf{c}}, \overline{\sigma})$ using density-weighted means:

$$\overline{\sigma} = \sum_{i \geq 0} \omega_i \sigma_i, \;\; \overline{\mathbf{c}} = \sum_{i \geq 0} \omega_i \mathbf{c}_i, \;\; \text{where} \;\; \omega_i = \frac{\sigma_i}{\sum_{j \geq 0} \sigma_j}. \tag{6}$$

Finally, we compute the pixel color by volume rendering. Our pipeline is trivially differentiable, allowing backpropagation through all parameters simultaneously.

Discussion on extrinsics disentanglement. An object's canonical orientation is ambiguous without assuming its category (Wang et al., 2019). Thus, we choose not to disentangle objects' orientation since we target category-agnostic object discovery. Further, we observe that uOCF has learned meaningful representations that can smoothly interpolate an object's scale and orientation. Please refer to Appendix B for visualization and analysis.

3.3 Object Prior Learning

Unsupervised discovery of 3D objects in complex scenes is inherently difficult due to multiple challenging ambiguities. A major ambiguity is what defines an object. While existing methods define objects via visual appearance similarity (Yu et al., 2022) or priors from 2D segments (Chen et al., 2024), they suffer from under-segmentation due to visual cluttering (Yu et al., 2022) or over-segmentation inherited from the 2D supervision (Chen et al., 2024).

We explore addressing this challenge by learning 3D object priors from synthetic data. Existing methods have difficulties learning generalizable 3D object priors, as their object representation is sensitive to spatial configurations: a minor shift in camera pose or object location, rather than the object itself, can lead to drastic changes in the object representation. Thus, such learned object priors do not generalize when there are unseen spatial configurations.

Our 3D object-centric representation mitigates this issue by translation invariance. In particular, we introduce 3D object prior learning. We show an illustration in Figure 3. The main idea is to pre-train uOCF on synthetic scenes that are constructed with a single object to ease the learning, similar to curriculum learning. After the pre-training stage, we proceed to training uOCF on the more complex scenes that may have different

(a) Room-Texture (b) Room-Furniture (c) Kitchen-Matte (d) Kitchen-Shiny

Figure 4: Samples from our datasets.

Table 1: Object segmentation and view synthesis on Room-Texture and Room-Furniture.

Method	Room-Texture						Room-Furniture					
	Object segmentation			Novel view synthesis			Object segmentation			Novel view synthesis		
	ARI↑	FG-ARI↑	NV-ARI↑	PSNR↑	SSIM↑	LPIPS↓	ARI↑	FG-ARI↑	NV-ARI↑	PSNR↑	SSIM↑	LPIPS↓
uORF (Yu et al., 2022)	0.670	0.093	0.578	24.23	0.711	0.254	0.686	0.497	0.556	27.49	0.780	0.258
BO-QSA (Jia et al., 2023)	0.697	0.354	0.604	25.26	0.739	0.215	0.682	0.479	0.579	27.29	0.774	0.261
COLF (Smith et al., 2023)	0.235	0.532	0.011	22.98	0.670	0.504	0.514	0.458	0.439	28.73	0.781	0.386
uOCF (ours)	**0.785**	**0.563**	**0.704**	**28.85**	**0.798**	**0.136**	**0.861**	**0.739**	**0.808**	**29.77**	**0.830**	**0.127**

object categories and spatial layouts. Note that either training stage does not require any object annotation. The pre-training synthetic single-object dataset can be easily scaled up.

3.4 Model Training

Object-centric sampling. To improve the reconstruction quality, we leverage an object's local coordinates to concentrate the sampled points in proximity to the object. Specifically, we start dropping distant samples from the predicted object positions after a few training epochs when the model has learned to distinguish the foreground objects and predict their positions. This approach enables us to quadruple the number of samples with the same amount of computation, leading to significantly improved robustness and visual quality.

In both training stages, we train our model across scenes, each with calibrated sparse multi-view images. For each training step, the model receives an image as input, infers the objects' latent representations and positions, renders multiple views from the input and reference poses, and compares them to the ground truth images to calculate the loss. Model supervision consists of the MSE reconstruction loss ℓ_{recon} and the perceptual loss ℓ_{perc} (Johnson et al., 2016) between the reconstructed and ground truth images. In addition, we incorporate the depth ranking loss (Wang et al., 2023a) with pre-trained monocular depth estimators and background occlusion regularization (Yang et al., 2023) to minimize common floating artifacts in few-shot NeRFs.

The overall loss function is thus formulated as follows:

$$\mathcal{L} = \ell_{\text{recon}} + \lambda_{\text{perc}}\ell_{\text{perc}} + \lambda_{\text{depth}}\ell_{\text{depth}} + \lambda_{\text{occ}}\ell_{\text{occ}}. \tag{7}$$

We leave further architectural details and illustrations in Appendix C.1.

4 Experiments

We evaluate our method on unsupervised object segmentation in 3D, novel view synthesis, and scene manipulation in 3D. We briefly describe the data collection process and experimental configurations, and we leave more details in Appendices C.2 and C.3. We attach sample code and data in the supplementary material, and we will release full code and data.

Data. We collect two synthetic datasets and two real-world datasets to evaluate our method. We show samples of our datasets in Figure 4.

Room-Texture. Room-Texture involves 324 object models from the "armchair" category of the ABO (Collins et al., 2022) dataset. Each scene contains 2–4 objects set against a background randomly chosen from a collection of floor textures. We collect $5,000$ scenes for training and 100 for evaluation. Each scene is rendered from 4 directions toward the scene center.

Room-Furniture. In Room-Furniture, objects are chosen from $1,425$ ABO (Collins et al., 2022) object models, spanning across seven categories, including "bed", "cabinet", "chair", "dresser", "ottoman", "sofa", and "plant pot". Other configurations are the same as Room-Texture.

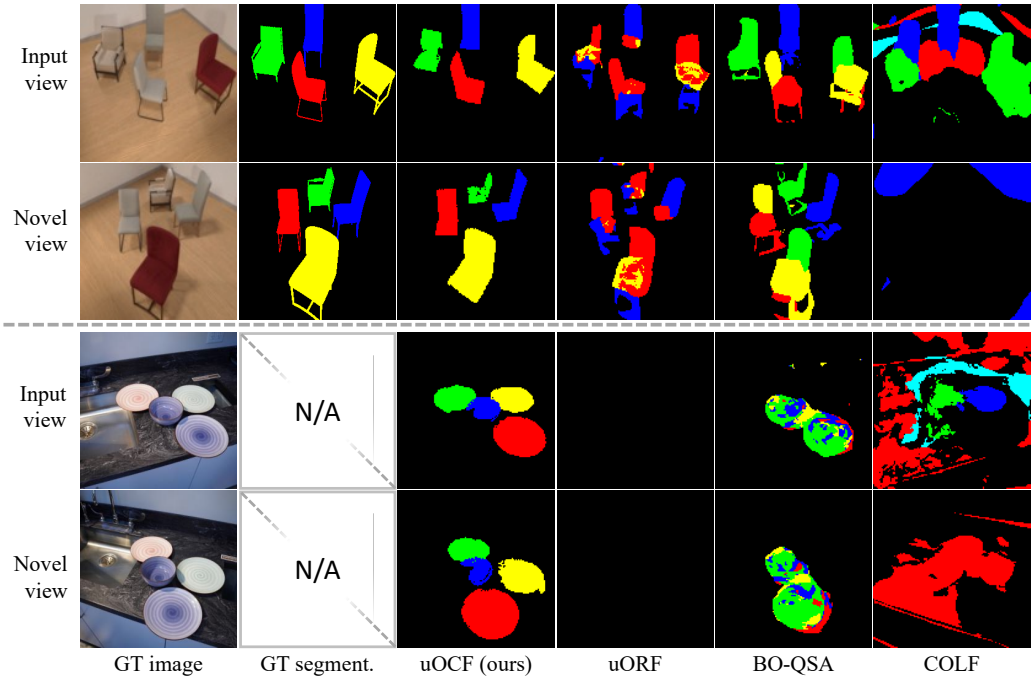

Figure 5: Scene segmentation qualitative results. Novel view images are for reference only.

Table 2: Novel view synthesis on Kitchen-Shiny and Kitchen-Matte.

Method	Kitchen-Shiny			Kitchen-Matte		
	PSNR↑	SSIM↑	LPIPS↓	PSNR↑	SSIM↑	LPIPS↓
uORF (Yu et al., 2022)	19.23	0.602	0.336	26.07	0.808	0.092
BO-QSA (Jia et al., 2023)	19.78	0.639	0.318	27.36	0.832	0.067
COLF (Smith et al., 2023)	18.30	0.561	0.397	20.68	0.643	0.236
uOCF (ours)	**28.58**	**0.862**	**0.049**	**29.40**	**0.867**	**0.043**

Table 3: Novel view synthesis on Kitchen-Shiny with a larger number of object queries K.

	PSNR↑	SSIM↑	LPIPS↓
$K = 4$	28.58	0.862	0.049
$K = 5$	28.28	0.846	0.059
$K = 6$	28.04	0.848	0.058
$K = 10$	28.20	0.840	0.065

Kitchen-Matte. This dataset features scenes with single-color matte dinnerware and two kinds of background environments: plain tabletop and complex kitchen backdrop. There are 735 scenes for training and 102 for evaluation. Each scene contains 3–4 objects at random positions and is captured from 3 poses (for tabletop scenes) or 2 poses (for kitchen backdrops).

Kitchen-Shiny. This dataset comprises scenes with textured shiny dinnerware. Similar to Kitchen-Matte, the first half presents a plain tabletop, while the latter has a kitchen background. There are 324 scenes for training and 56 for evaluation.

Details on the object prior learning. For the pre-training stage in our object prior learning, we generate a synthetic dataset of over $8,000$ scenes, where in each scene we place an object (sampled from a high-quality subset from Objaverse-LVIS (Deitke et al., 2023)) on a room background. These objects span across more than 100 categories. These synthetic data are easy to generate and scale up. We use this dataset for pre-training (object prior learning) on all our experiments.

Qualitative metrics. We report the PSNR, SSIM, and LPIPS metrics for novel view synthesis. For scene segmentation, we use three variants of the Adjusted Rand Index (ARI): the conventional ARI (calculated on all input image pixels), the Foreground ARI (FG-ARI, calculated on foreground input image pixels), and the Novel View ARI (NV-ARI, calculated on novel view pixels). For a fair comparison with prior methods, all scores are computed on images of resolution 128×128.

Baselines. We compare our method with uORF (Yu et al., 2022), BO-QSA (Jia et al., 2023), and COLF (Smith et al., 2023). We use the same evaluation protocol as in these prior works. We increase the

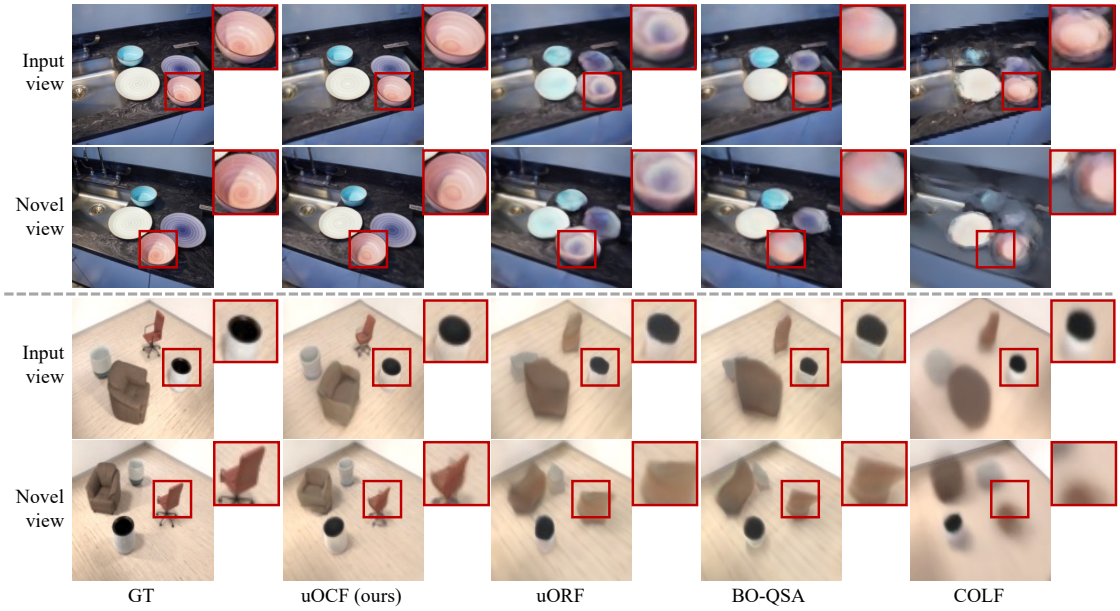

Figure 6: Novel view synthesis qualitative results on Kitchen-Shiny (top) and Room-Furniture (bottom).

Table 4: Scene manipulation results on Room-Texture.

Method	Object Translation			Object Removal		
	PSNR↑	SSIM↑	LPIPS↓	PSNR↑	SSIM↑	LPIPS↓
uORF (Yu et al., 2022)	23.65	0.654	0.284	23.81	0.664	0.282
BO-QSA (Jia et al., 2023)	25.21	0.700	0.226	24.58	0.698	0.247
uOCF (ours)	**27.66**	**0.774**	**0.156**	**28.99**	**0.802**	**0.136**

latent dimensions and training iterations for the baselines for fair comparisons. By default, we set the number of foreground object queries to $K = 4$ for all methods. At inference, each model takes the same single image from the test set as input and generates a set of discovered objects and background radiance fields. Note that all test scenes have different spatial configurations than the training scenes. We use all test images from all scenes and report the averaged numbers.

4.1 Baseline Comparison on Multiple Tasks

Unsupervised object segmentation in 3D. We evaluate the object discovery quality by object segmentation in 3D. We render a density map $\mathbf{d}^i$ for each latent i and assign each pixel p a segmentation label $s_p = \arg\max_{i=0}^{K} \mathbf{d}_p^i$ in the input view and novel views. We show our results in Table 1 and examples in Figure 5. From Table 1, we see that our uOCF outperforms all existing methods in all metrics. From Figure 5, we observe that no prior method can produce reasonable segmentation results in real-world Kitchen-Shiny scenes. Specifically, uORF binds all objects to the background, resulting in empty object segmentation; BO-QSA fails to distinguish different object instances; COLF produces meaningless results on novel views. A fundamental issue in these methods is that they lack appropriate object priors to handle the ambiguity in disentangling multiple objects. In contrast, uOCF can discover objects in real-world scenes. Moreover, uOCF can handle scenes where objects occlude each other. We provide more visualization results in Appendix D.

Novel view synthesis. We evaluate the scene and object reconstruction quality by novel view synthesis. For each test scene, we use a single image as input and other views as references. We show our results in Table 2 and examples in Figure 6. We also show additional results in Appendix D. Our method significantly surpasses the baselines in all metrics. Importantly, while previous methods often fail to distinguish foreground objects and thus produce blurry reconstruction of objects, our approach consistently produces high-fidelity scene and object reconstruction and novel view synthesis results.

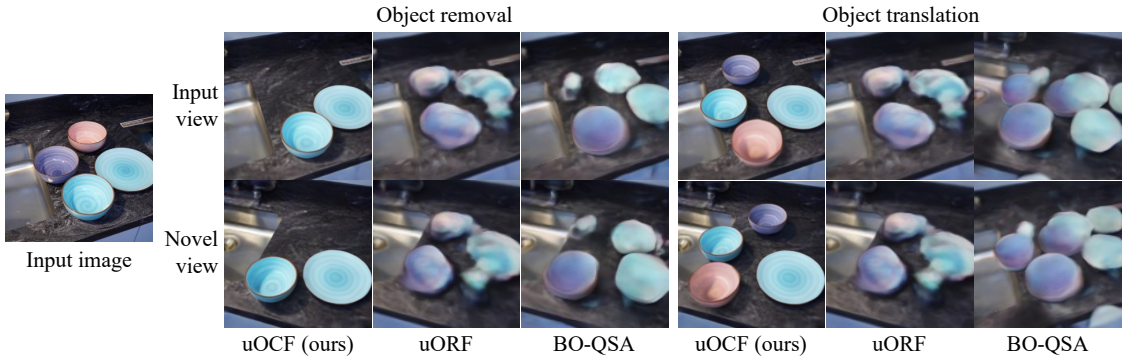

Figure 7: Qualitative results of single-image 3D scene manipulation.

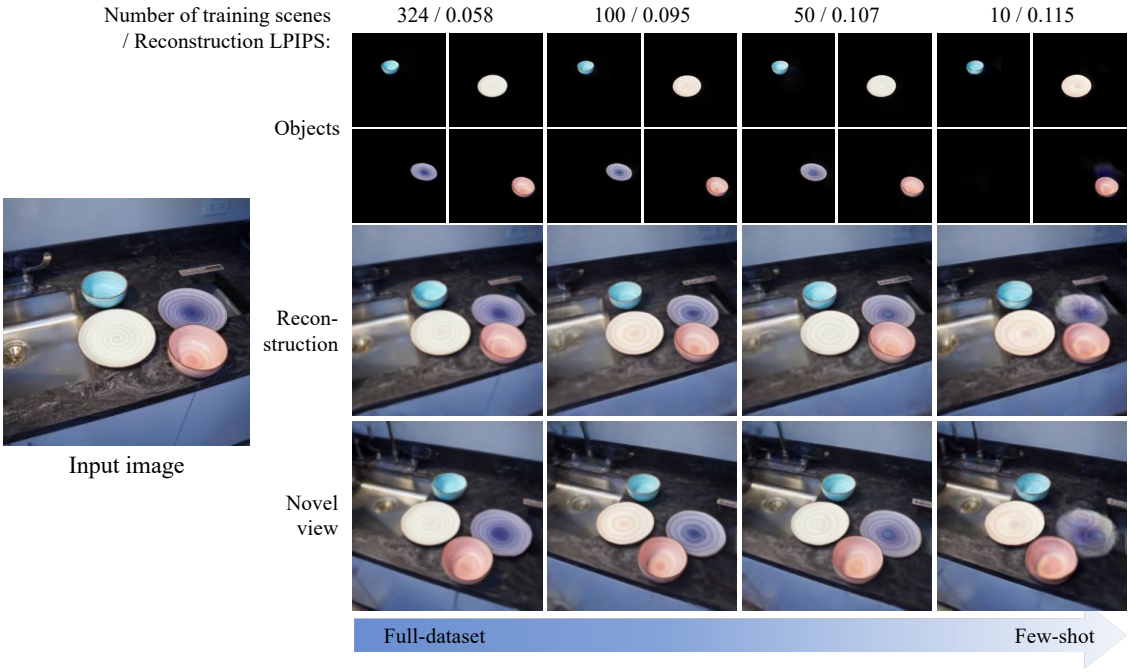

Figure 8: Qualitative results about sample efficiency. With less training scenes, our uOCF can still produce reasonable object discovery thank to the object-centric modeling and learned object priors.

Scene manipulation in 3D. We further evaluate object discovery by single-image 3D scene manipulation. Since uOCF explicitly infers 3D locations of discovered objects, it readily supports: 1) object translation by modifying an object's position, and 2) object removal by excluding objects during compositional rendering.

For quantitative evaluation, we create a test set by randomly selecting an object in each of the Room-Texturescenes, and shift its position (object translation) or remove it (object removal). During inference, we determine the object to manipulate by selecting the object with the highest IoU score with the ground truth mask. As shown in Table 4, uOCF outperforms baselines across all metrics in both object translation and object removal due to its better performance in object discovery. We further show qualitative examples from the Kitchen-Shiny dataset in Figure 7. We observe that uORF merges all objects into the background, and thus the manipulation results are identical to the original reconstruction; BO-QSA fails to distinguish foreground objects, resulting in blurry manipulation results (we show more visualization in Appendix D). In contrast, our uOCF delivers much higher-quality manipulation results. We show additional visualization results in the supplementary video.

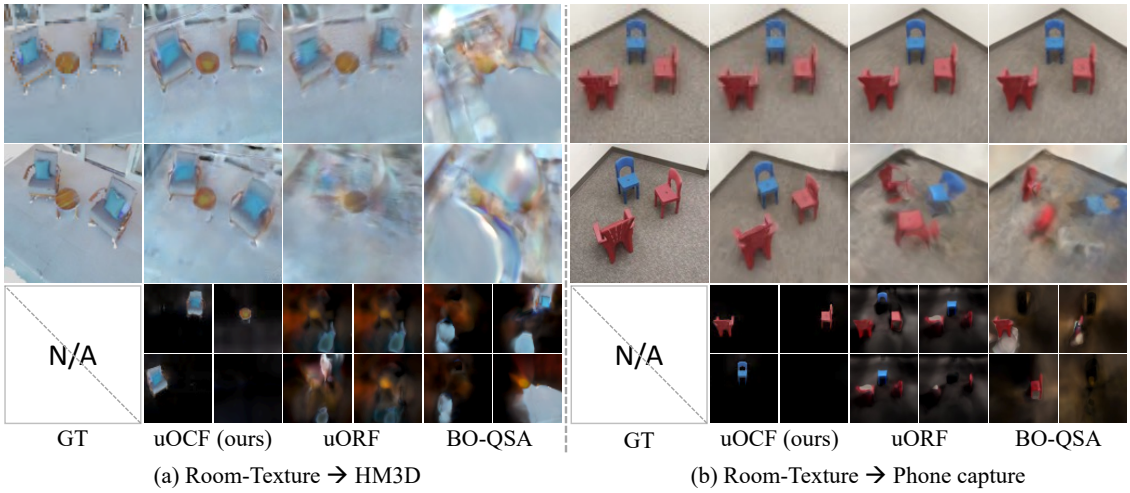

Figure 9: Zero-shot generalization results. We load the model trained on one dataset and test it on an image from another dataset after a fast test-time optimization using a photometric reconstruction loss on the *input view only*. First/second/third row: scene reconstruction/novel view/objects.

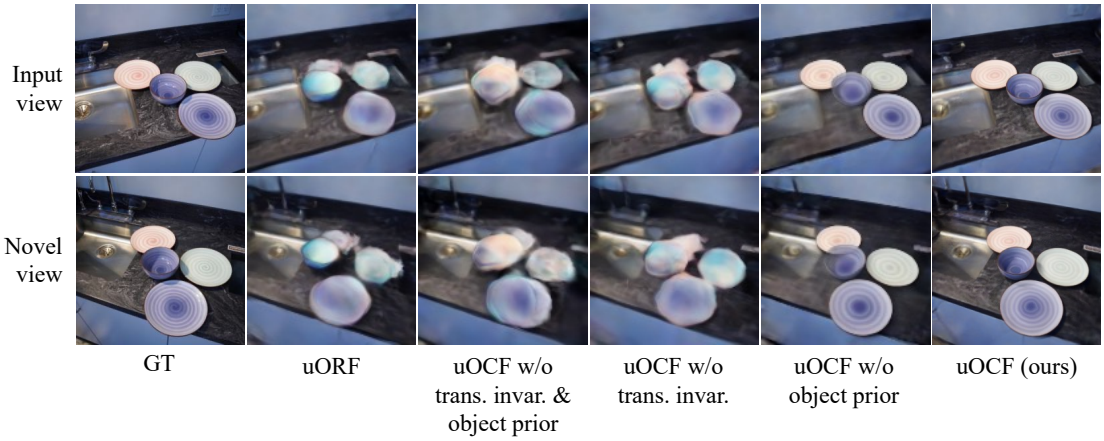

Figure 10: Ablation on the key technical contributions: translation invariance and object prior learning.

4.2 Generalization Analysis

In the experiments above, all test scenes have unseen novel spatial configurations, where uOCF shows strong generalization. We further evaluate the sample efficiency on spatial generalization, and we showcase the generalization to unseen objects.

Sample efficiency. We train uOCF with a small subset of (e.g., only 10) the training scenes, and test it on the test set. As shown by the qualitative example in Figure 8, even when we only have a few training scenes, uOCF still demonstrates a good generalization ability to discover objects. This is mainly due to the translation invariance and learned object priors, which reduce the dependence on massive training scenes.

Generalization to unseen objects. We evaluate the zero-shot generalization ability of uOCF by training it on one dataset and test it on a single image of unseen background and objects. In particular, we test our method on two real-world examples (one from the HM3D dataset (Ramakrishnan et al., 2021) and the other from a cellphone capture), adapting the model trained on only the synthetic Room-Texture dataset. We show the qualitative results in Figure 9. We observe that while all existing methods struggle to adapt to unseen objects, uOCF exhibits remarkable generalization. It requires only a minimal single-image test-time optimization to adapt from one synthetic dataset to real-world images with unseen objects.

Table 5: Ablation studies on our key technical contributions on Kitchen-Shiny.

Method	PSNR ↑	SSIM ↑	LPIPS ↓
w/o trans. invar. or object prior learning	20.68	0.645	0.303
w/o trans. invar.	23.70	0.724	0.186
w/o object prior learning	26.81	0.806	0.125
uOCF (ours)	**28.58**	**0.862**	**0.049**

Table 6: Ablation study on model architecture and loss function on Kitchen-Shiny.

Method	PSNR↑	SSIM↑	LPIPS↓
w/o DINO	26.25	0.831	0.060
w/o standard attention	27.82	0.844	0.062
w/o object-centric sampling	27.31	0.852	0.072
w/o ℓ_{depth} and ℓ_{occ}	26.79	0.819	0.081
uOCF (ours)	**28.58**	**0.862**	**0.049**

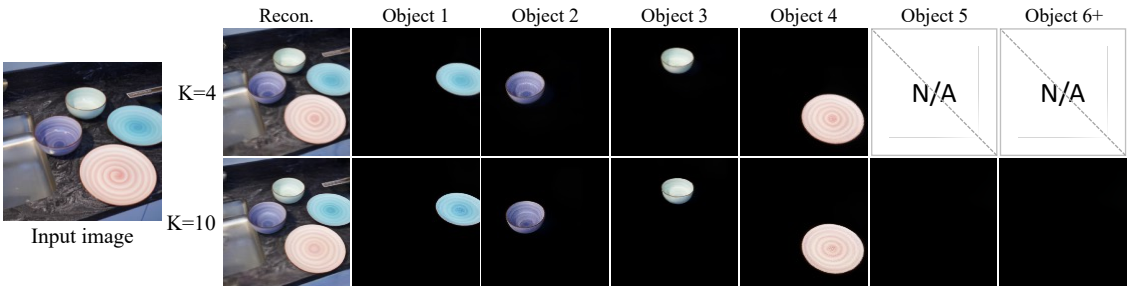

Figure 11: Qualitative results of uOCF on scenes with larger object queries K. The order of the object reconstructions is rearranged for better visualization.

4.3 Ablation Study

Key technical contributions. We first present ablation studies on our key technical contributions, namely the translation-invariant design and the object prior learning.

As shown in Table 5 and Figure 10, incorporating translation invariance would significantly decrease LPIPS from 0.186 to 0.049, and leveraging object prior learning would notably decrease LPIPS from 0.125 to 0.049. Both our technical contributions, namely translation invariance and object prior learning, are complementary-important, as removing both significantly hurts performances.

Other technical improvements. We also present ablation studies on the technical improvements. As shown in Table 6, the introduction of DINO ViT and standard attention improves overall performance, yet they give relatively minor contributions to the performances (e.g., removing DINO or standard attention only slightly increases LPIPS from 0.049 to 0.060 or 0.062). Similarly, excluding the depth and occlusion losses degrades the visual quality, resulting in a performance drop. Meanwhile, removing the object-centric sampling strategy slightly degrades the overall reconstruction quality.

Different K values. We evaluate the effectiveness of different K values and different scales of data used for 3D object prior learning. We evaluate our method's robustness to different K values, and we show results in Table 3 and Figure 11. From Table 3, we can see that even when we set $K = 10$ which is much higher than the number of possible maximal objects (i.e., 4), our model is robust and gives comparable results. From Figure 11, we observe that even if there are more object queries than the number of objects in the scene, uOCF learns to generate "empty" object queries instead of over-segmenting the objects.

5 Conclusion

We study the importance of translation invariance for unsupervised 3D object discovery, instantiated as our model for the unsupervised discovery of Object-Centric neural Fields (uOCF). Our results show that our translation-invariant design and the 3D object prior learning can substantially improve the spatial generalization and sample efficiency. Our results demonstrate that unsupervised 3D object discovery can be extended to real scenes while obtaining satisfactory performances.

Limitations. Although uOCF shows promising unsupervised 3D object discovery results, it is currently limited to simple real scenes such as the kitchen scenes. Extending to more complex real scenes with complex spatial layouts and a large number of objects from different categories is an important future direction. We leave more discussion on technical limitations in Appendix E.

References

Jonathan T Barron, Ben Mildenhall, Matthew Tancik, Peter Hedman, Ricardo Martin-Brualla, and Pratul P Srinivasan. Mip-nerf: A multiscale representation for anti-aliasing neural radiance fields. In *IEEE/CVF International Conference on Computer Vision (ICCV)*, 2021.

Ondrej Biza, Sjoerd van Steenkiste, Mehdi SM Sajjadi, Gamaleldin F Elsayed, Aravindh Mahendran, and Thomas Kipf. Invariant slot attention: Object discovery with slot-centric reference frames. In *International Conference on Machine Learning (ICML)*, 2023.

Christopher P Burgess, Loic Matthey, Nicholas Watters, Rishabh Kabra, Irina Higgins, Matt Botvinick, and Alexander Lerchner. Monet: Unsupervised scene decomposition and representation. *arXiv:1901.11390*, 2019.

Jiazhong Cen, Jiemin Fang, Chen Yang, Lingxi Xie, Xiaopeng Zhang, Wei Shen, and Qi Tian. Segment any 3d gaussians. *arXiv:2312.00860*, 2023a.

Jiazhong Cen, Zanwei Zhou, Jiemin Fang, Wei Shen, Lingxi Xie, Xiaopeng Zhang, and Qi Tian. Segment anything in 3d with nerfs. In *Advances in Neural Information Processing Systems (NeurIPS)*, 2023b.

Chang Chen, Fei Deng, and Sungjin Ahn. Learning to infer 3d object models from images. *arXiv:2006.06130*, 2020.

Honglin Chen, Wanhee Lee, Hong-Xing Yu, Rahul Mysore Venkatesh, Joshua B Tenenbaum, Daniel Bear, Jiajun Wu, and Daniel LK Yamins. Unsupervised 3d scene representation learning via movable object inference. *Transactions on Machine Learning Research (TMLR)*, 2024.

Jasmine Collins, Shubham Goel, Kenan Deng, Achleshwar Luthra, Leon Xu, Erhan Gundogdu, Xi Zhang, Tomas F Yago Vicente, Thomas Dideriksen, Himanshu Arora, Matthieu Guillaumin, and Jitendra Malik. Abo: Dataset and benchmarks for real-world 3d object understanding. In *IEEE/CVF Conference on Computer Vision and Pattern Recognition (CVPR)*, 2022.

Eric Crawford and Joelle Pineau. Spatially invariant unsupervised object detection with convolutional neural networks. In *AAAI Conference on Artificial Intelligence (AAAI)*, 2019.

Matt Deitke, Dustin Schwenk, Jordi Salvador, Luca Weihs, Oscar Michel, Eli VanderBilt, Ludwig Schmidt, Kiana Ehsani, Aniruddha Kembhavi, and Ali Farhadi. Objaverse: A universe of annotated 3d objects. In *IEEE/CVF Conference on Computer Vision and Pattern Recognition (CVPR)*, 2023.

Aniket Didolkar, Anirudh Goyal, and Yoshua Bengio. Cycle consistency driven object discovery. *arXiv:2306.02204*, 2023.

Martin Engelcke, Adam R Kosiorek, Oiwi Parker Jones, and Ingmar Posner. Genesis: Generative scene inference and sampling with object-centric latent representations. *arXiv:1907.13052*, 2019.

SM Eslami, Nicolas Heess, Theophane Weber, Yuval Tassa, David Szepesvari, Koray Kavukcuoglu, and Geoffrey E Hinton. Attend, infer, repeat: Fast scene understanding with generative models. In *Advances in Neural Information Processing Systems (NeurIPS)*, 2016.

SM Ali Eslami, Danilo Jimenez Rezende, Frederic Besse, Fabio Viola, Ari S Morcos, Marta Garnelo, Avraham Ruderman, Andrei A Rusu, Ivo Danihelka, Karol Gregor, et al. Neural scene representation and rendering. *Science*, 2018.

Zhiwen Fan, Peihao Wang, Yifan Jiang, Xinyu Gong, Dejia Xu, and Zhangyang Wang. Nerf-sos: Any-view self-supervised object segmentation on complex scenes. *arXiv:2209.08776*, 2022.

Kristen Grauman and Trevor Darrell. Unsupervised learning of categories from sets of partially matching image features. In *IEEE/CVF Conference on Computer Vision and Pattern Recognition (CVPR)*, 2006.

Klaus Greff, Antti Rasmus, Mathias Berglund, Tele Hotloo Hao, Jürgen Schmidhuber, and Harri Valpola. Tagger: Deep unsupervised perceptual grouping. In *Advances in Neural Information Processing Systems (NeurIPS)*, 2016.

Klaus Greff, Sjoerd Van Steenkiste, and Jürgen Schmidhuber. Neural expectation maximization. In *Advances in Neural Information Processing Systems (NeurIPS)*, 2017.

Klaus Greff, Raphaël Lopez Kaufman, Rishabh Kabra, Nick Watters, Christopher Burgess, Daniel Zoran, Loic Matthey, Matthew Botvinick, and Alexander Lerchner. Multi-object representation learning with iterative variational inference. In *International Conference on Machine Learning (ICML)*, 2019.

Yicong Hong, Kai Zhang, Jiuxiang Gu, Sai Bi, Yang Zhou, Difan Liu, Feng Liu, Kalyan Sunkavalli, Trung Bui, and Hao Tan. Lrm: Large reconstruction model for single image to 3d. *arXiv preprint arXiv:2311.04400*, 2023.

Baoxiong Jia, Yu Liu, and Siyuan Huang. Improving object-centric learning with query optimization. In *International Conference on Learning Representations (ICLR)*, 2023.

Jindong Jiang, Sepehr Janghorbani, Gerard de Melo, and Sungjin Ahn. Scalor: Generative world models with scalable object representations. In *International Conference on Learning Representations (ICLR)*, 2020.

Justin Johnson, Alexandre Alahi, and Li Fei-Fei. Perceptual losses for real-time style transfer and super-resolution. In *European Conference on Computer Vision (ECCV)*, 2016.

Armand Joulin, Francis Bach, and Jean Ponce. Discriminative clustering for image co-segmentation. In *IEEE/CVF Conference on Computer Vision and Pattern Recognition (CVPR)*, 2010.

Adam R Kosiorek, Hyunjik Kim, Ingmar Posner, and Yee Whye Teh. Sequential attend, infer, repeat: Generative modelling of moving objects. In *Advances in Neural Information Processing Systems (NeurIPS)*, 2018.

Abhijit Kundu, Yin Li, and James M Rehg. 3d-rcnn: Instance-level 3d object reconstruction via render-and-compare. In *IEEE/CVF Conference on Computer Vision and Pattern Recognition (CVPR)*, 2018.

Bo Li, Zhengxing Sun, Qian Li, Yunjie Wu, and Anqi Hu. Group-wise deep object co-segmentation with co-attention recurrent neural network. In *IEEE/CVF Conference on Computer Vision and Pattern Recognition (CVPR)*, 2019.

Shengnan Liang, Yichen Liu, Shangzhe Wu, Yu-Wing Tai, and Chi-Keung Tang. Onerf: Unsupervised 3d object segmentation from multiple views. *arXiv:2211.12038*, 2022.

Zhixuan Lin, Yi-Fu Wu, Skand Vishwanath Peri, Weihao Sun, Gautam Singh, Fei Deng, Jindong Jiang, and Sungjin Ahn. Space: Unsupervised object-oriented scene representation via spatial attention and decomposition. In *International Conference on Learning Representations (ICLR)*, 2020.

Francesco Locatello, Dirk Weissenborn, Thomas Unterthiner, Aravindh Mahendran, Georg Heigold, Jakob Uszkoreit, Alexey Dosovitskiy, and Thomas Kipf. Object-centric learning with slot attention. In *Advances in Neural Information Processing Systems (NeurIPS)*, 2020.

Ben Mildenhall, Pratul P Srinivasan, Matthew Tancik, Jonathan T Barron, Ravi Ramamoorthi, and Ren Ng. Nerf: Representing scenes as neural radiance fields for view synthesis. In *European Conference on Computer Vision (ECCV)*, 2020.

Tom Monnier, Elliot Vincent, Jean Ponce, and Mathieu Aubry. Unsupervised layered image decomposition into object prototypes. In *IEEE/CVF International Conference on Computer Vision (ICCV)*, 2021.

Norman Müller, Andrea Simonelli, Lorenzo Porzi, Samuel Rota Bulo, Matthias Nießner, and Peter Kontschieder. Autorf: Learning 3d object radiance fields from single view observations. In *IEEE/CVF Conference on Computer Vision and Pattern Recognition (CVPR)*, 2022.

Thu H Nguyen-Phuoc, Christian Richardt, Long Mai, Yongliang Yang, and Niloy Mitra. Blockgan: Learning 3d object-aware scene representations from unlabelled images. In *Advances in Neural Information Processing Systems (NeurIPS)*, 2020.

Michael Niemeyer and Andreas Geiger. Giraffe: Representing scenes as compositional generative neural feature fields. In *IEEE/CVF Conference on Computer Vision and Pattern Recognition (CVPR)*, 2021.

Maxime Oquab, Timothée Darcet, Théo Moutakanni, Huy Vo, Marc Szafraniec, Vasil Khalidov, Pierre Fernandez, Daniel Haziza, Francisco Massa, Alaaeldin El-Nouby, et al. Dinov2: Learning robust visual features without supervision. *arXiv:2304.07193*, 2023.

Julian Ost, Fahim Mannan, Nils Thuerey, Julian Knodt, and Felix Heide. Neural scene graphs for dynamic scenes. In *IEEE/CVF Conference on Computer Vision and Pattern Recognition (CVPR)*, 2021.

Jeong Joon Park, Peter Florence, Julian Straub, Richard Newcombe, and Steven Lovegrove. Deepsdf: Learning continuous signed distance functions for shape representation. In *IEEE/CVF Conference on Computer Vision and Pattern Recognition (CVPR)*, 2019.

Santhosh K Ramakrishnan, Aaron Gokaslan, Erik Wijmans, Oleksandr Maksymets, Alex Clegg, John Turner, Eric Undersander, Wojciech Galuba, Andrew Westbury, Angel X Chang, et al. Habitat-matterport 3d dataset (hm3d): 1000 large-scale 3d environments for embodied ai. *arXiv:2109.08238*, 2021.

René Ranftl, Katrin Lasinger, David Hafner, Konrad Schindler, and Vladlen Koltun. Towards robust monocular depth estimation: Mixing datasets for zero-shot cross-dataset transfer. *Transactions on Pattern Analysis and Machine Intelligence (TPAMI)*, 2022.

Bryan C Russell, William T Freeman, Alexei A Efros, Josef Sivic, and Andrew Zisserman. Using multiple segmentations to discover objects and their extent in image collections. In *IEEE/CVF Conference on Computer Vision and Pattern Recognition (CVPR)*, 2006.

Mehdi SM Sajjadi, Daniel Duckworth, Aravindh Mahendran, Sjoerd van Steenkiste, Filip Pavetic, Mario Lucic, Leonidas J Guibas, Klaus Greff, and Thomas Kipf. Object scene representation transformer. In *Advances in Neural Information Processing Systems (NeurIPS)*, 2022.

Vincent Sitzmann, Michael Zollhöfer, and Gordon Wetzstein. Scene representation networks: Continuous 3d-structure-aware neural scene representations. In *Advances in Neural Information Processing Systems (NeurIPS)*, 2019.

Josef Sivic, Bryan C Russell, Alexei A Efros, Andrew Zisserman, and William T Freeman. Discovering objects and their location in images. In *IEEE/CVF International Conference on Computer Vision (ICCV)*, 2005.

Cameron Smith, Hong-Xing Yu, Sergey Zakharov, Fredo Durand, Joshua B Tenenbaum, Jiajun Wu, and Vincent Sitzmann. Unsupervised discovery and composition of object light fields. *Transactions on Machine Learning Research (TMLR)*, 2023.

Karl Stelzner, Kristian Kersting, and Adam R Kosiorek. Decomposing 3d scenes into objects via unsupervised volume segmentation. *arXiv:2104.01148*, 2021.

Ayush Tewari, Ohad Fried, Justus Thies, Vincent Sitzmann, Stephen Lombardi, Kalyan Sunkavalli, Ricardo Martin-Brualla, Tomas Simon, Jason Saragih, Matthias Nießner, et al. State of the art on neural rendering. *Computer Graphics Forum*, 2020.

Huy V Vo, Patrick Pérez, and Jean Ponce. Toward unsupervised, multi-object discovery in large-scale image collections. In *European Conference on Computer Vision (ECCV)*, 2020.

Guangcong Wang, Zhaoxi Chen, Chen Change Loy, and Ziwei Liu. Sparsenerf: Distilling depth ranking for few-shot novel view synthesis. In *IEEE/CVF International Conference on Computer Vision (ICCV)*, 2023a.

He Wang, Srinath Sridhar, Jingwei Huang, Julien Valentin, Shuran Song, and Leonidas J Guibas. Normalized object coordinate space for category-level 6d object pose and size estimation. In *IEEE/CVF Conference on Computer Vision and Pattern Recognition (CVPR)*, 2019.

Qian Wang, Yiqun Wang, Michael Birsak, and Peter Wonka. Blobgan-3d: A spatially-disentangled 3d-aware generative model for indoor scenes. *arXiv:2303.14706*, 2023b.

Jiajun Wu, Joshua B Tenenbaum, and Pushmeet Kohli. Neural scene de-rendering. In *IEEE/CVF Conference on Computer Vision and Pattern Recognition (CVPR)*, 2017.

Qianyi Wu, Xian Liu, Yuedong Chen, Kejie Li, Chuanxia Zheng, Jianfei Cai, and Jianmin Zheng. Object-compositional neural implicit surfaces. In *European Conference on Computer Vision (ECCV)*, 2022.

Yiheng Xie, Towaki Takikawa, Shunsuke Saito, Or Litany, Shiqin Yan, Numair Khan, Federico Tombari, James Tompkin, Vincent Sitzmann, and Srinath Sridhar. Neural fields in visual computing and beyond. *Computer Graphics Forum*, 2022.

Bangbang Yang, Yinda Zhang, Yinghao Xu, Yijin Li, Han Zhou, Hujun Bao, Guofeng Zhang, and Zhaopeng Cui. Learning object-compositional neural radiance field for editable scene rendering. In *IEEE/CVF Conference on Computer Vision and Pattern Recognition (CVPR)*, 2021.

Jiawei Yang, Marco Pavone, and Yue Wang. Freenerf: Improving few-shot neural rendering with free frequency regularization. In *IEEE/CVF Conference on Computer Vision and Pattern Recognition (CVPR)*, 2023.

Shunyu Yao, Tzu Ming Harry Hsu, Jun-Yan Zhu, Jiajun Wu, Antonio Torralba, William T Freeman, and Joshua B Tenenbaum. 3d-aware scene manipulation via inverse graphics. In *Advances in Neural Information Processing Systems (NeurIPS)*, 2018.

Alex Yu, Vickie Ye, Matthew Tancik, and Angjoo Kanazawa. pixelnerf: Neural radiance fields from one or few images. In *IEEE/CVF Conference on Computer Vision and Pattern Recognition (CVPR)*, 2021.

Hong-Xing Yu, Leonidas J Guibas, and Jiajun Wu. Unsupervised discovery of object radiance fields. In *International Conference on Learning Representations (ICLR)*, 2022.

A Appendix Overview

This supplementary document is structured as follows: We begin with the proof of concept in Appendix B and provide the implementation details in Appendix C. Then, we discuss the limitations of our approach in Appendix E and present additional qualitative results in Appendix D. Accompanying this document is our *project page with an overview video* attached in the supplementary file.

B Proof of Concept

We conduct a toy experiment (Figure 12) to demonstrate that our model has successfully learned object position, rotation, and scale. In this experiment, we begin with two images (input 1 and input 2) of a chair placed at the scene's center, exhibiting different sizes (on the left) or rotation angles (on the right), all captured from the same viewing direction.

We extract the object latents from these images, interpolate them, and then send the interpolated latents to the decoder. As shown between the two input images, we observe a smooth transition in object size and rotation, indicating that the latent representation has effectively captured the scale and rotation of objects.

In the second row, we placed the chairs in different positions. As shown on the right, we obtained a smooth transition again, proving that our model could disentangle object positions from the latent representation.

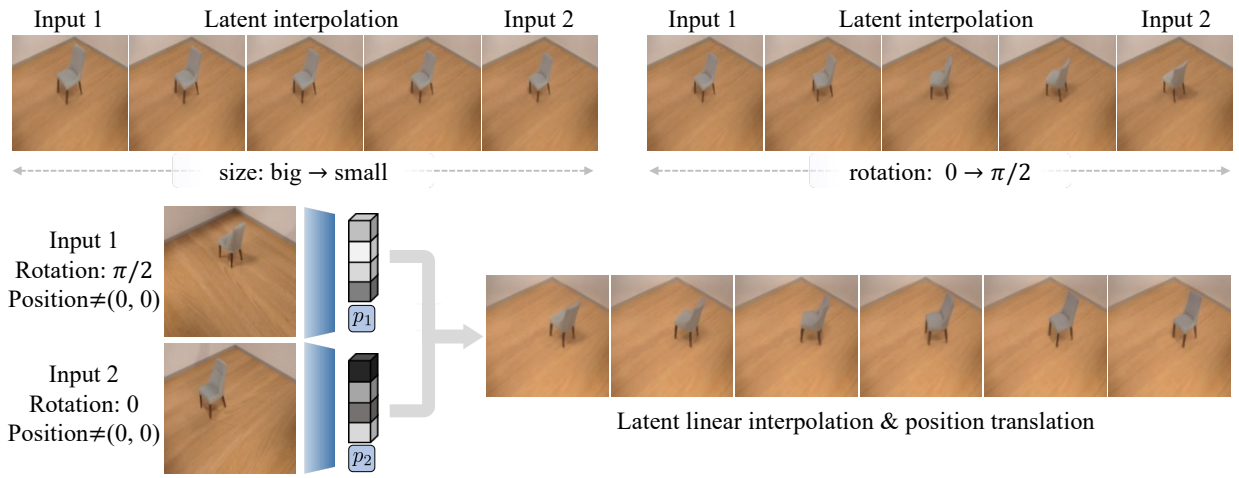

Figure 12: Proof of concept. We demonstrate that uOCF has effectively learned objects' scale and orientation along with the translation-invariant object representation by interpolating the representation of two identical objects with different orientations and scales to obtain transitional results.

C Implementation

C.1 Model Architecture

Encoder. Our encoder module consists of a frozen DINO encoder and two convolutional layers. We illustrate its architecture in Figure 13(a).

Latent Inference Module. While motivated by the background-aware slot attention module proposed by (Yu et al., 2022), our latent inference module exhibits three key differences: (1) The object queries are initialized with learnable embeddings instead of being sampled from learnable Gaussians, which enhances training stability; (2) We jointly extract object positions and their latent representations and add object-specific positional encoding to utilize the extracted position information; (3) We remove the Gated Recurrent Unit (GRU) and replace it with the transformer architecture to smooth the gradient flow.

C.2 Data Collection

This section introduces the details of our datasets.

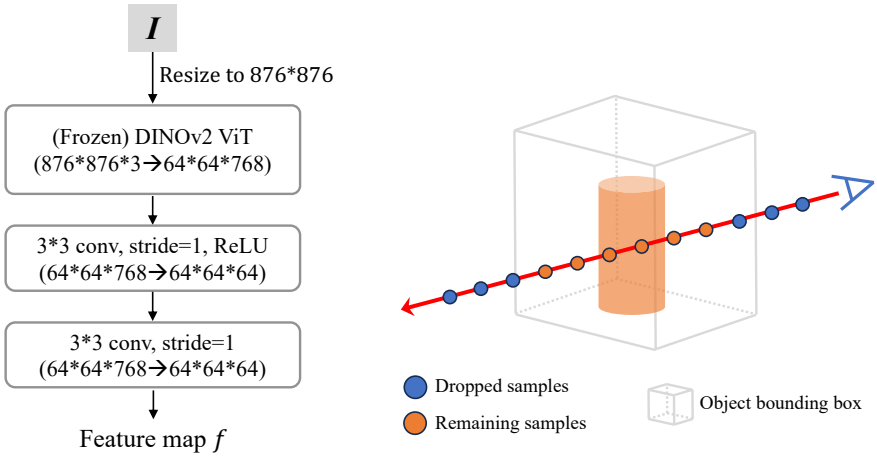

(a) Encoder architecture (b) Object-centric sampling

Figure 13: (a) Architecture of our encoder module. (b) Object-centric sampling: We drop the samples distant from the predicted object position for efficient sampling..

Room-Texture. In Room-Texture, objects are chosen from 324 ABO objects (Collins et al., 2022) from the "armchair" category. The single-object subset contains four scenes for each object instance, resulting in 1296 scenes in total. The multiple-object subset includes $5,000$ scenes for training and 100 for evaluation, with each scene containing 2-4 objects set against a background randomly chosen from a collection of floor textures. Each scene is rendered from 4 directions toward the center.

Room-Furniture. In Room-Furniture, objects are chosen from $1,425$ ABO (Collins et al., 2022) object models, spanning across seven categories, including "bed", "cabinet", "chair", "dresser", "ottoman", "sofa", and "plant pot". Each scene contains 2-4 objects set against a background randomly chosen from a collection of floor textures. We render 5000 scenes for training and 100 scenes for evaluation.

Kitchen-Matte. In Kitchen-Matte, objects are diffuse and have no texture. The dataset comprises 16 objects and 6 tablecloths in total. We captured 3 images for each tabletop scene and 2 for each kitchen scene. This dataset contains 735 scenes for training and 102 for evaluation, each containing 3-4 objects. We calibrate the cameras using the OpenCV library.

Kitchen-Shiny. In Kitchen-Shiny, objects are specular, and the lighting is more complex. The dataset comprises 12 objects and 6 tablecloths, and the other settings are identical to Kitchen-Matte. This dataset contains 324 scenes for training and 56 for evaluation, each containing 4 objects.

C.3 Training Configuration

This section discusses the training configuration of uOCF.

We employ Mip-NeRF (Barron et al., 2021) as our NeRF backbone and estimate the depth maps by MiDaS (Ranftl et al., 2022). An Adam optimizer with default hyper-parameters and an exponential decay scheduler is used across all experiments. The initial learning rate is 0.0003 for the first stage and 0.00015 for the second stage. Loss weights are set to $\lambda_{\text{perc}} = 0.006, \lambda_{\text{depth}} = 1.5$, and $\lambda_{\text{occ}} = 0.1$. The position update momentum m is set to 0.5, and the latent inference module lasts $T = 6$ iterations. All experiments are run on a single RTX-A6000 GPU.

Coarse-To-Fine Progressive Training. We employ a coarse-to-fine strategy in our second training stage to facilitate training at higher resolutions. Reference images are downsampled to a lower resolution (64×64) during the coarse training stage and replaced by image patches with the same size as the low-resolution images randomly cropped from the high-resolution (128×128) input images during the fine training stage.

Locality Constraint and Object-Centric Sampling. We employ the locality constraint (a bounding box for foreground objects in the world coordinate) proposed by (Yu et al., 2022) in both training stages but only adopt it before starting object-centric sampling. The number of samples along each ray before and after starting object-centric sampling is set to 64 and 256, respectively. We provide an illustration of our object-centric sampling strategy in Figure 13(b).

Training Configuration on Room-Texture. During stage 1, we train the model for 100 epochs directly on images of resolution 128×128. We start with the reconstruction loss only, add the perceptual 10^{th} epoch, and start the object-centric sampling at the 20^{th} epoch. During stage 2, we train the model for 60 epochs on the coarse stage and another 60 on the fine stage. We start with the reconstruction loss only, add the perceptual loss at the 10^{th} epoch, and start the object-centric sampling from the 20^{th} epoch.

Training Configuration on Kitchen-Matte and Kitchen-Shiny. Both kitchen datasets share the same training configuration with Room-Texture in stage 1. During stage 2, we train the model for 750 epochs, where the fine stage starts at the 250^{th} epoch. We add the perceptual loss at the 50^{th} epoch and start the object-centric sampling from the 150^{th} epoch.

D Additional Qualitative Results

Visualization on Discovered Objects. We visualize the discovered objects in Figure 14. Notably, uORF (Yu et al., 2022) puts all objects within the background, whereas BO-QSA (Jia et al., 2023) binds the same object to all queries, resulting in identical foreground reconstruction. In contrast, uOCF accurately differentiates between the foreground objects and the background.

Visualization on Object Segmentation in 3D. We show scene segmentation results on the kitchen datasets in Figure 15. Unlike compared methods that yield cluttered results, uOCF consistently yields high-fidelity segmentation results.

Additional Novel View Synthesis Results. We show more qualitative results for novel view synthesis in Figures 15, 16, and 17. Our method produces much better results than compared methods regarding visual quality.

E Limitations Analysis

Limitation on Reconstruction Quality. Scene-level generalizable NeRFs (Yu et al., 2021; Sajjadi et al., 2022; Yu et al., 2022) commonly face challenges in accurately reconstructing detailed object textures. Our approach also has difficulty capturing extremely high-frequency details. As shown in Figure 18(a), our method fails to replicate the mug's detailed texture. Future research may benefit from stronger object priors learned from larger-scale datasets, such as Large Reconstruction Models (Hong et al., 2023).

Failure in Position Prediction. Our two-stage training pipeline, despite its robustness in many situations, is not immune to errors, particularly in object position prediction. Due to the occlusion between objects, using the attention-weighted mean for determining object positions can sometimes lead to inaccuracies. Although a bias term can rectify this in most instances (Figure 6), discrepancies persist under a few conditions, as depicted in Figure 18(b).

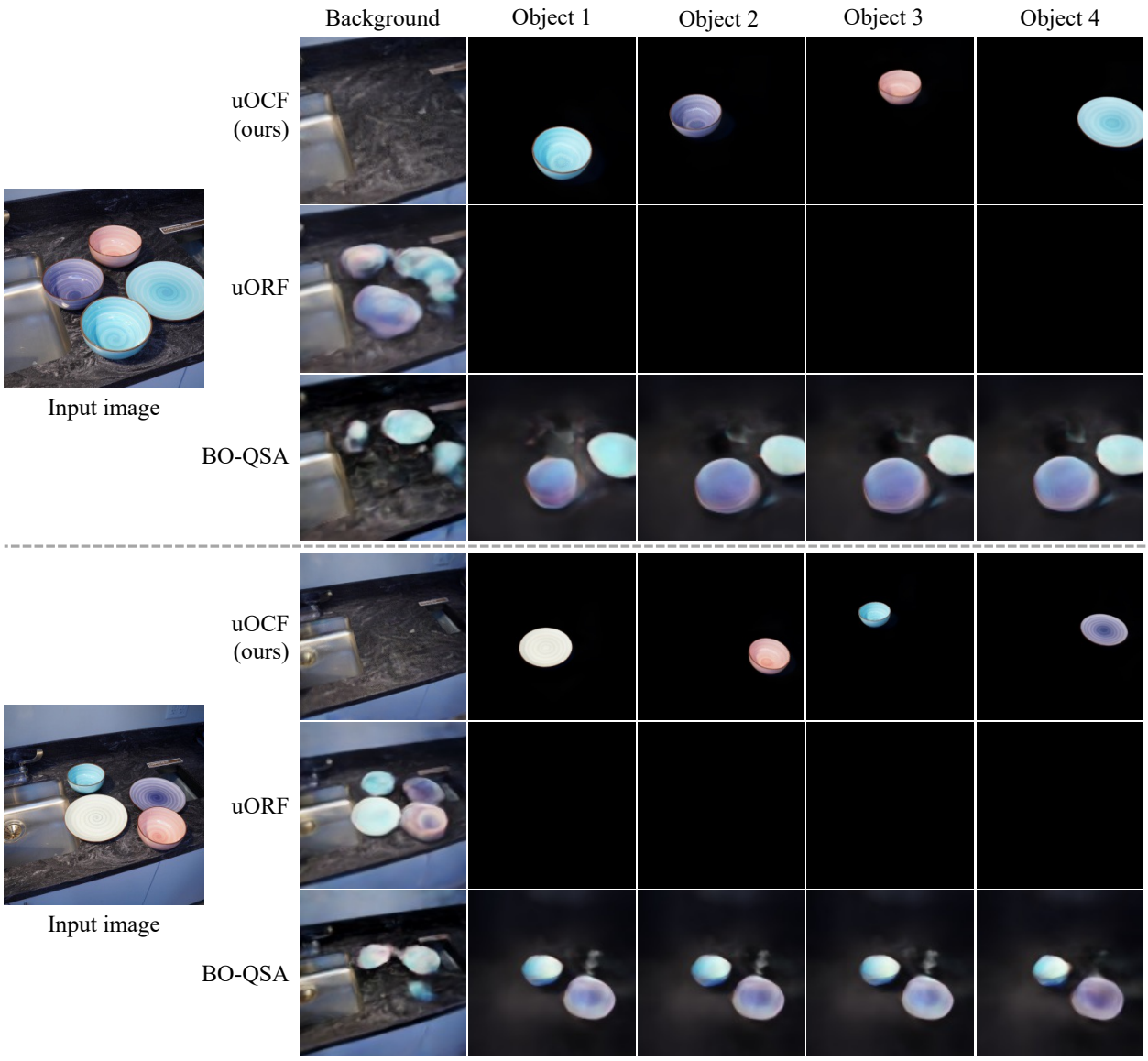

Figure 14: Visualization on discovered objects on Kitchen-Shiny.

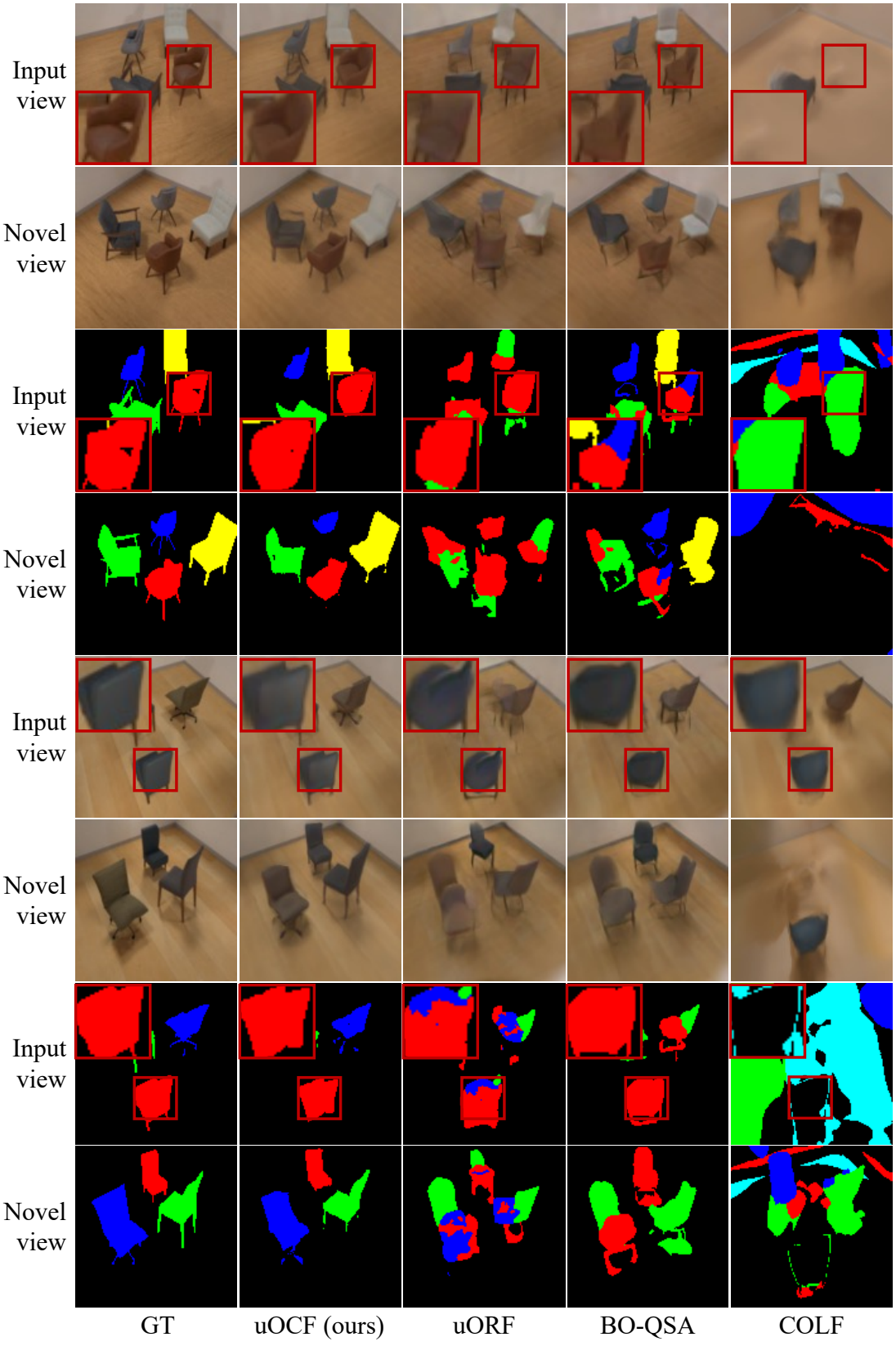

Figure 15: Additional segmentation and view synthesis results on the Room-Texture dataset.

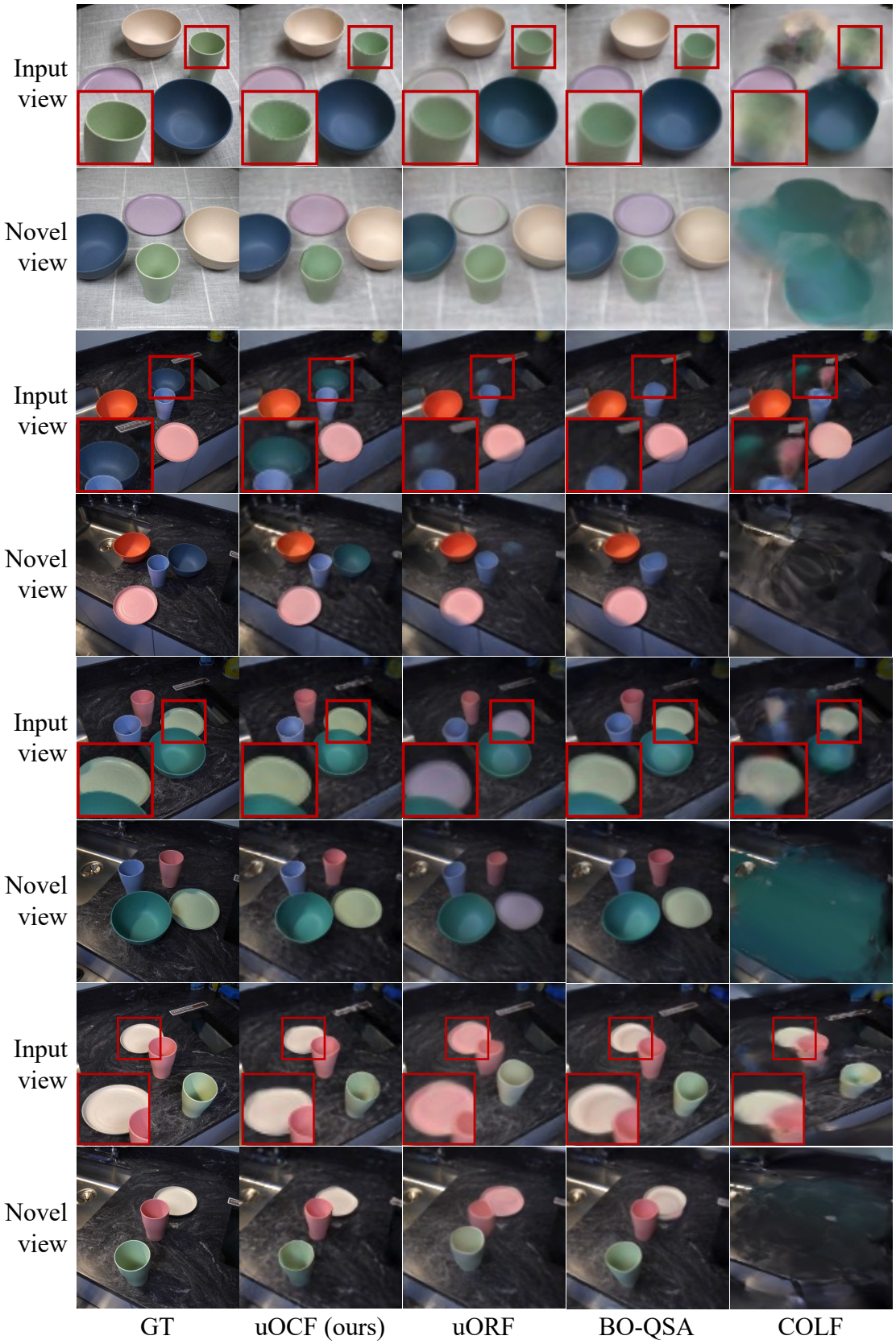

Figure 16: Additional view synthesis results on the Kitchen-Matte dataset.

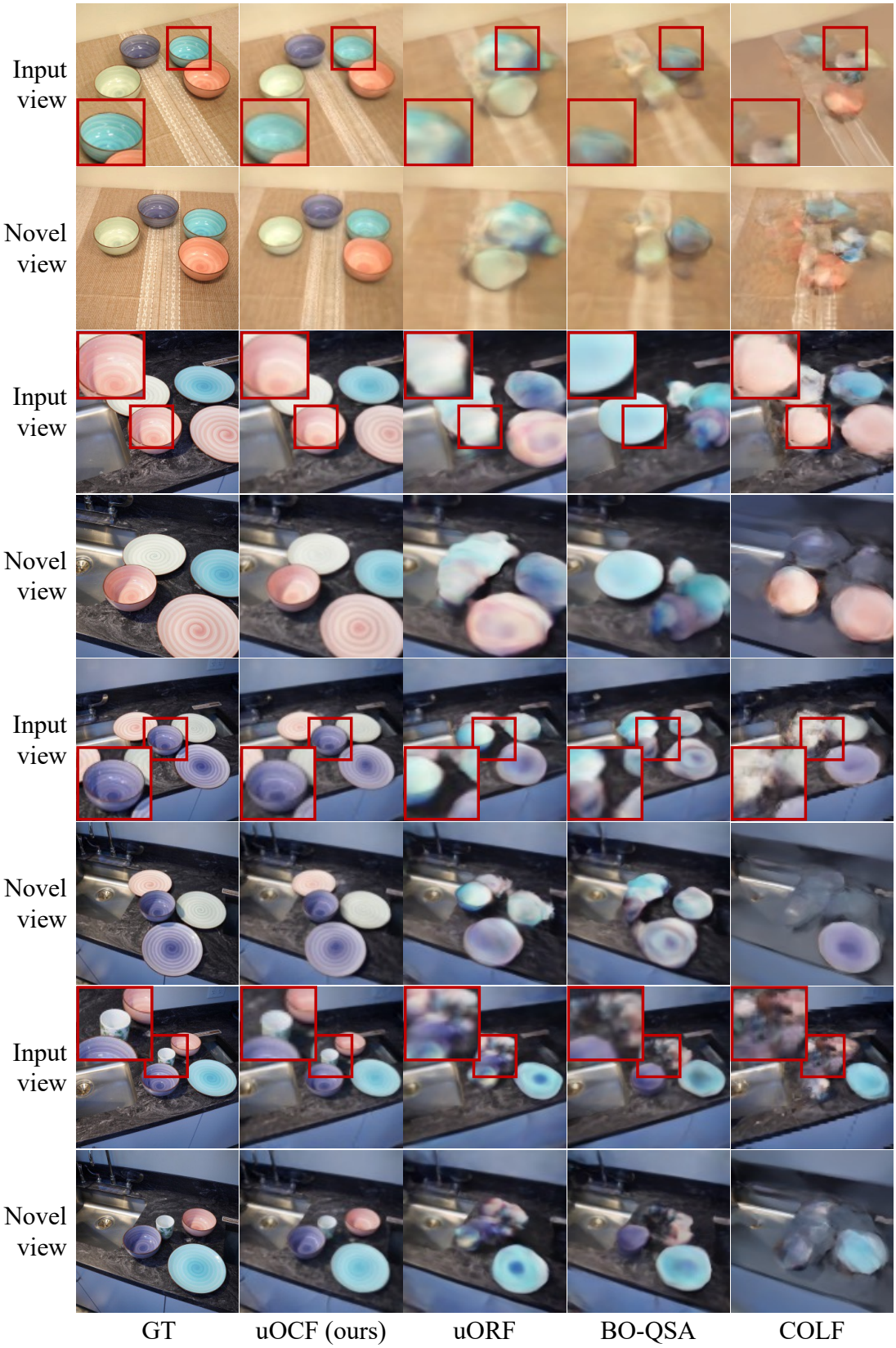

Figure 17: Additional view synthesis results on the Kitchen-Shiny dataset.

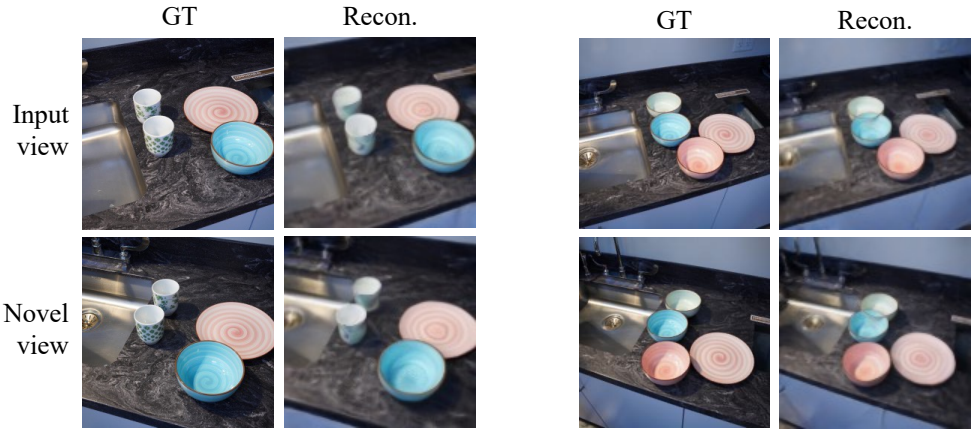

Figure 18: Failure case visualizations. Our method may fail to reconstruct intricate object texture or predict biased object position.